

Stochastic Properties of Minimal Arc Distance and Cosine Similarity between a Random Point and Prespecified Sites on Sphere

Hongjun Li^a, Jiatong Sui^b, Shengpeng Mu^a, Xing Qiu^{b,*}

^a*College of Science, Beijing Forestry University, Beijing, China*

^b*Department of Biostatistics and Computational Biology, University of Rochester, New York, U.S.A.*

Abstract

In applications such as wireless communication, it is important to study the statistical properties of L_2 , the minimal arc distance between a random point (e.g., a cellphone user) uniformly distributed on a sphere to a set of pre-defined seeds (e.g., wireless towers) on that sphere. In this study, we first derive the distribution (CDF) and density (PDF) functions of the arc distance between a selected vertex of a spherical triangle to a random point uniformly distributed within this triangle. Next, using computational techniques based on spherical Voronoi diagram and triangular partition of Voronoi cells, we derive moments of L_2 and $\cos L_2$. These results are verified by extensive Monte Carlo simulations.

Keywords: Arc distance, cosine similarity, distribution function, moments, spherical geometry, Voronoi diagram

1. Introduction

A Voronoi diagram, also known as Thiessen polygon or Dirichlet tessellation, is a powerful tool in conducting research related to the partition of a space [1]. Given a set of pre-specified points (called seeds or sites), a Voronoi diagram

*Correspondence should be send to: Xing Qiu.

Email addresses: lihongjun69@bjfu.edu.cn (Hongjun Li), jiatong\$_sui@urmc.rochester.edu (Jiatong Sui), Shengpengmu@bjfu.edu.cn (Shengpeng Mu), xing\$_qiu@urmc.rochester.edu (Xing Qiu)

divides the space into regions (called Voronoi cells) according to the nearest-neighbor rule, such that each region contains exactly one seed and the interior points of the regions are closer to this seed than any others [2, 3].

Voronoi diagrams can be constructed efficiently [4], and it has wide applications in various disciplines, including forestry, chemistry, transportation, and statistics [5, 6, 7, 8]. In particular, it has been used by mathematicians and statisticians to model stochastic foam geometries [9], estimating Shannon entropy of multidimensional probability [10], approximating resampling-based distributions [11], etc.

In this study, we focus on the following application of Voronoi diagram in wireless communications. As we know, wireless signal strength depends critically on the distance between a user's device (e.g., cell phone) and the *nearest* base station. In order to study the distribution and moments of this minimal distance, we need to decompose the whole region covered by wireless signal into Voronoi cells [12, 13] of which the seeds are base stations. Because a Voronoi cell is a convex polygon composed of several triangles intersecting at the seed, it suffices to study the stochastic properties of the distance between a selected vertex (the seed) of a triangle and a random interior point. Several research teams, including us, have study this problem on \mathbb{R}^2 thoroughly under the assumption that the random point follows a uniform distribution on the triangle [14, 15, 16, 13]. In particular, we derived the closed-form cumulative distribution function (CDF), probability density function (PDF), and the first two moments of this random distance [13].

There are various generalizations of Voronoi diagram that serve better for certain applications [17], including higher order diagrams, weighted Voronoi diagrams, and the case in which the seeds are replaced by line segments [18, 12, 19, 20]. Another large class of generalizations are Voronoi diagrams defined on non-Euclidean geometric spaces, e.g., Laguerre planes or spheres [21, 22, 23]. The latter case (spherical Voronoi diagram, illustrated in Figure 1) is especially important in practice, not least because the Earth is approximated spherical. Again take the wireless communication problem as an example, if the base

stations to be modeled occupy a relatively large area, using the spherical Voronoi diagram defined on S^2 would be more accurate than the planar Voronoi diagram. There are similar problems in large-scale forest ecology, vehicle distribution management, and biomolecular structure modeling, that can benefit from using the spherical rather than planar Voronoi diagram.

The distance between random points on S^2 have been studied by a few researchers, including the generation and test of uniformity on the sphere [24], minimization of the summation of Euclidean distances of n random points [25], and random spherical packing [26, 27]. However, no prior studies have systematically studied the stochastic properties of $L_0(\Delta PBC)$, the random *spherical distance* (*a.k.a.* arc distance) between a given vertex P to a random point Q which is uniformly distributed on the spherical triangle ΔPBC .

In this study, we first study the stochastic properties of $L_0(\Delta PBC)$ in detail, and extend these results to the case in which the spherical triangle ΔPBC is replaced by an arbitrary convex spherical polygon. Next, we use these results and techniques based on spherical Voronoi diagram to derive the distribution of $L_2(P_1, \dots, P_m)$, which is the minimal arc distance between a uniformly distributed random point on S^2 to $\{P_1, \dots, P_m\}$, a collection of pre-specified sites on the same sphere.

This manuscript is organized as follows. In Section 2 we provide useful preliminary results about spherical triangles. Detailed derivations of the CDF and PDF of $L_0(\Delta PBC)$, as well as their generalizations to convex spherical polygons (dubbed as $L_1(\Gamma, P)$, where Γ is a convex spherical polygon and P is an arbitrary internal seed), are given in Sections 3.1 and 3.2. The CDF and PDF of $L_2(P_1, \dots, P_m)$ is derived in Section 3.3. The close-form expression of first four moments of $L_0(\Delta PBC)$ is provided in Section 4. To further demonstrate the utility of the CDF and PDF derived in Section 3, we derive the exact formula for several moments of $\cos(L_0(\Delta PBC))$ in Appendix B. These quantities are useful in spherical cluster analysis and data mining [28, 29, 30, 31].

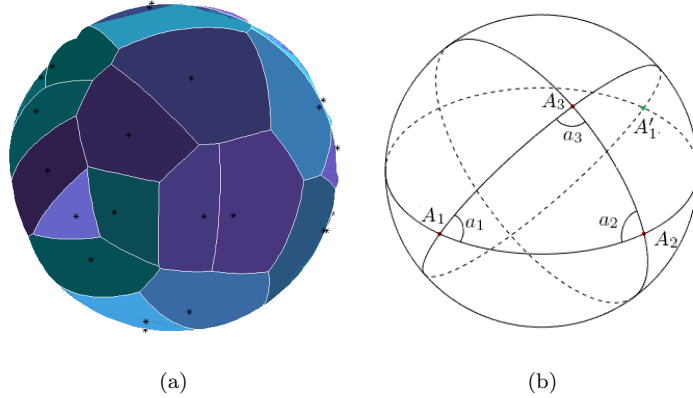


Figure 1: An illustration of spherical Voronoi diagram and spherical triangles. (a) Given a set of seeds, the spherical Voronoi diagram is a partition of a sphere into convex spherical polygons, such that the points within each polygon has the shortest spherical (angular) distance to the interior seed than all exterior seeds. A combination of triangulation and mid-point bisector inspector is employed to form these honeycomb-like, asymmetric, mesh-like shapes. (b) Due to the non-Euclidean nature of S^2 , a “straight line” (geodesic) on S^2 is a great circle, and the spherical triangle is a triangular shaped area enclosed by three great circles. The spherical distance between two points such as A_1 and A_2 is measured by the arc-length of the great circle passing through these two points. Spherical geometry and trigonometry is fundamentally different from planar geometry/trigonometry. For instance, the sum of the interior angles of a spherical triangle exceeds 180 degrees [32].

2. Useful geometric properties of spherical triangles

Throughout this manuscript, we denote the sphere in \mathbb{R}^3 centered at the origin (denoted by O) with radius R by $S_R^2 := \{x \in \mathbb{R}^2 : |x| = R\}$. Let A and B be two distinct and non-opposing points on S_R^2 , e.g., $A \neq \pm B$, they define a great circle, i.e., geodesic on S_R^2 . We denote the smallest arc of a great circle with endpoints A and B by L_{AB} ; $\angle AOB$ measured in radians by φ_{AB} . We also denote the area of the spherical cap by A_{cap} and the half-of-top angle [16] of this spherical cap by θ (see Fig. 2(a)). The area of a spherical sector, as shown in Fig. 2(b), is denoted by A_{fan} , its top angle is denoted by α . Formal definitions of these concepts can be found in Appendix A.

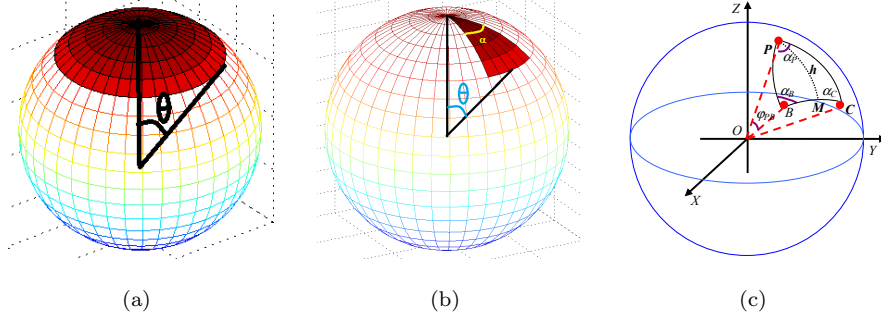


Figure 2: The three sub-figures illustrate the cap, fan and triangle on a sphere. (a) A spherical cap is the region of a sphere cut off by a plane. If the plane passes through the center of the sphere, the cap is called a hemisphere. We could use a second plane to cut the cap, which will result in a spherical segment. (b) A spherical fan on the sphere is part of a spherical cap generated by further partitions, using great circles passing through the apex or the pole of spherical cap. (c) A triangle from a sphere can be formed using 3 points on a sphere, connected by the great circles. In this paper, we consider the inner triangles instead of the outer triangles. The sum of the angles of an inner spherical triangle is between π and 3π times the radius.

Area of spherical triangle. Let $\alpha_P, \alpha_B, \alpha_C$ be the three interior angles of triangle ΔPBC , as shown in Fig. 2(c). It is well known that the area of ΔPBC is

$$A_{\Delta} = R^2(\alpha_P + \alpha_B + \alpha_C - \pi) = R^2 E \quad (1)$$

Here α_P, α_B , and α_C represent angles between great circles. The spherical angle $\angle APB = \alpha$ can be calculated with the following Equation

$$\alpha = \arccos((\vec{OA} \times \vec{OP})^0 \cdot (\vec{OB} \times \vec{OP})^0) \quad (2)$$

Here \vec{v}^0 represents the unit direction of vector $v \in \mathbb{R}^3$, namely, $\vec{v}^0 := \vec{v}/|\vec{v}|$.

The calculation for α_B and α_C are similar. E is called the *spherical excess*, $0 \leq E \leq 2\pi$, with $E = 0$ being the degenerate case in which all three points locate on one great circle.

Altitude of spherical triangle. An important concept used in our derivation is the *altitude* of a spherical triangle, which is a generalization of the altitude of a planar triangle [13]. For spherical triangle ΔPBC , the length h_{BC} (or h) of

the altitude to base edge \widehat{BC} is the length of arc \widehat{PM} , as shown in Fig. 2(c), which can be calculated as

$$h = R \angle POM = R \arcsin(\vec{n} \cdot \overrightarrow{OP}^0) \quad (3)$$

where \vec{n} is the unit normal direction of the plane defined by points O, B and C : $\vec{n} := (\overrightarrow{OB} \times \overrightarrow{OC})^0$; h is the shortest distance from vertex P to the greatest circle defined by B and C . In addition, the intersection M can be calculated by the following equation

$$\overrightarrow{OM} = R(\overrightarrow{OP} + t\vec{n}), \quad (4)$$

where $t := -(\vec{n} \cdot \overrightarrow{OP})$.

3. Distribution of the Minimal Arc Distance

In this section, we will derive the distribution of $L_2(P_1, \dots, P_m)$, the minimal arc distance between a random point Q to a pre-specified set of sites $\{P_1, \dots, P_m\}$ on a sphere.

3.1. Distribution of $L_0(\Delta PBC)$

Recall that ΔPBC is an arbitrary spherical triangle, and $L_0(\Delta PBC)$ represents the arc distance between P to a random point Q uniformly distributed in ΔPBC . Without loss of generality, we may choose B and C such that that $L_{PB} \leq L_{PC}$. In [16], Ahmadi and Pan classified every spherical triangle ΔPBC into two cases based on whether the altitude from P to the arc BC is inside (e.g., Fig.3(a)) or outside (e.g., Fig.3(b)) of the triangle.

We find that these two cases based on the altitude can be unified into a single graph (Fig.3(c)) as follows: based on the altitude, a reflection of arc PB about the altitude is drawn. The outside and the inside arcs are denoted by \widehat{PB}_1 and \widehat{PB}_2 , respectively. Then for the inside-altitude case, B coincides with B_1 , while for the outside-altitude case, B coincides with B_2 . The above procedure is illustrated in Fig. 3(c).

The altitude length h can be calculated with Equation (3). $F_{L_0}(r)$, the CDF of L_0 can be represented as $F_{L_0}(r) = S(r)/\Omega$, where Ω is the area of the

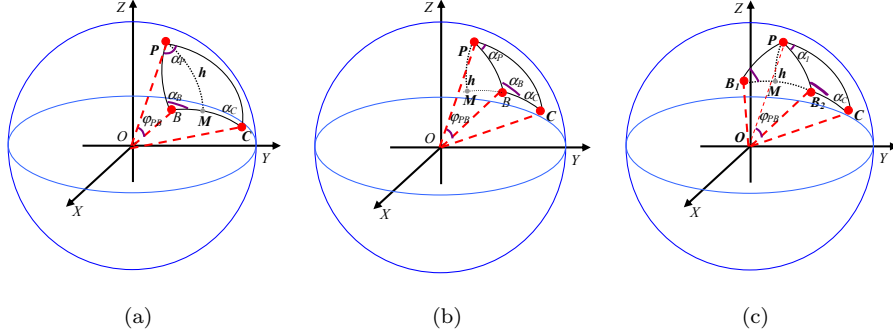


Figure 3: ΔPBC can be classified into two classes based on the location of the altitude PM : (a) The inside-altitude case, $PM \subset \Delta PBC$, (b) the outside-altitude case, $PM \not\subset \Delta PBC$. By reflecting arc PB about the altitude PM , we can unify these two cases, which is illustrated in (c).

spherical triangle ΔPBC and $S(r) := |B_r(P) \cap \Delta PBC|$ [15], where $B_r(P)$ is a spherical cap centered at P with radius r . By construction, $B_r(P) \cap \Delta PBC$ contains those points in ΔPBC with arc distance to P less or equal to r . The following four cases need to be considered.

Case 1. When $0 < r \leq h$, $B_r(P) \cap \Delta PBC$ is a sector, centered at P , with two cut points on $\widehat{PB_1}$ and \widehat{PC} , as shown in Fig.4(a). Using Equation (A.3), its area is

$$S(r) = \alpha_P(1 - \cos r)R^2, \quad (5)$$

where α_P is $\angle BPC$.

Case 2. When $h < r \leq L_{PB}$, $B_r(P) \cap \Delta PBC$ consists of a spherical triangle, ΔPD_1D_2 (mid), and two sectors, (both centered at P , one has cut points on $\widehat{PB_1}$ and $\widehat{PD_1}$, the other cuts on $\widehat{PD_2}$ and \widehat{PC}), as shown in Fig.4(b). With Equations (A.3) and (1), we have

$$S(r) = \{\alpha_1(1 - \cos r) + \eta[(\pi/2 + \alpha_r + \beta_r - \pi) + (\alpha_2 - \alpha_r)(1 - \cos r)]\}R^2. \quad (6)$$

Here $\alpha_r = \angle MPD_2$, $\beta_r = \angle PD_2M$, and their values depend on r . $\alpha_1 = \angle CPB_2$ and $\alpha_2 = \angle MPB_2$ do not depend on r . $\eta := L_{BB_2}/L_{MB_2}$, thus $\eta = 0$ if $B = B_2$, $\eta = 2$ if $B = B_1$.

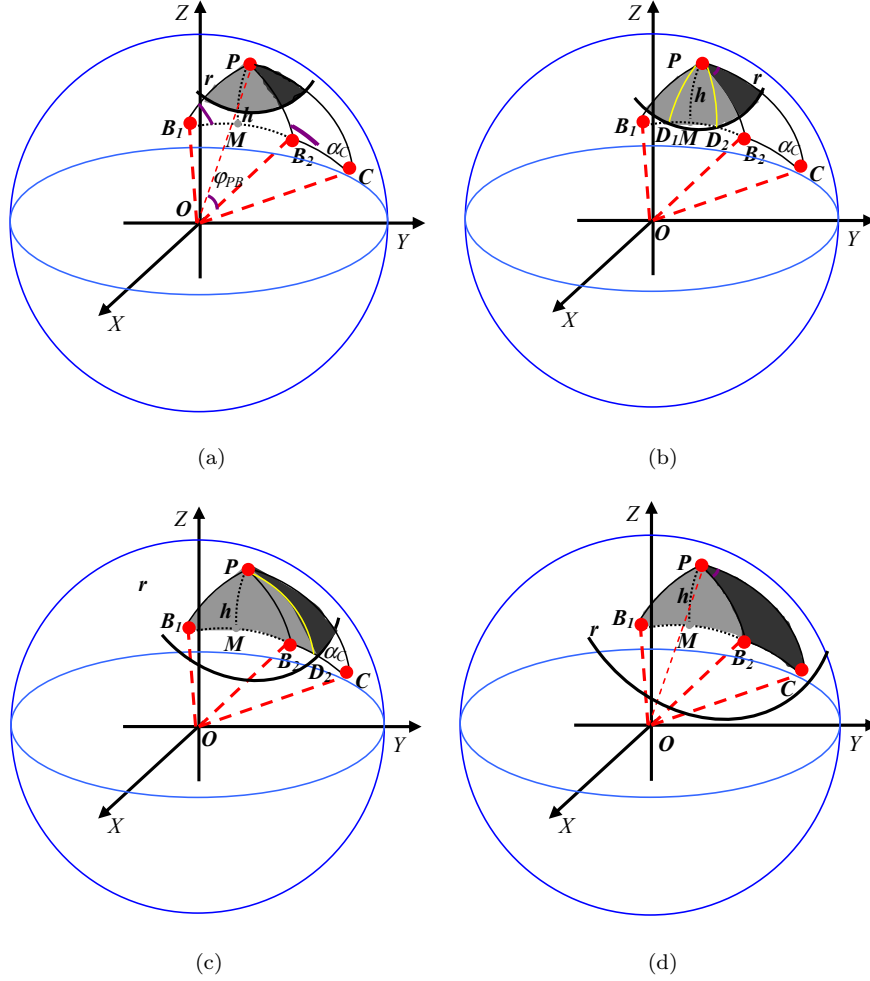


Figure 4: The CDF/PDF of $r_0(\Delta PBC)$ depends on how the spherical fan originated from P with radius r intersects with ΔPBC . By construction, every point P in this fan satisfies $L_{PQ} \leq r$, therefore $P(r_0 \leq r)$ is the ratio between the area of the intersection and the area of the triangle. This intersection can be classified as follows: (a) case 1: $0 < r_0 \leq h$, the intersection is a sector. (b) case 2: $h < r_0 \leq L_{PB}$, it contains a spherical triangle and two sectors. (c) case 3: $L_{PB} < r_0 \leq L_{PC}$, it contains a spherical triangle and a sector. (d) case 4: $r_0 > L_{PC}$, it is a spherical triangle.

α_r and β_r can be represented in one integrative Equation (6) for both inside-

altitude and outside-altitude cases

$$\alpha_r = \cos^{-1}[(\overrightarrow{OM} \times \overrightarrow{OP})^0 \cdot (\overrightarrow{OD_2} \times \overrightarrow{OP})^0] \quad (7)$$

$$= \arccos\left(\frac{\tan h}{\tan r}\right). \quad (8)$$

$$\beta_r = \cos^{-1}[(\overrightarrow{OP} \times \overrightarrow{OD_2})^0 \cdot (\overrightarrow{OM} \times \overrightarrow{OD_2})^0] \quad (9)$$

$$= \arcsin\left(\frac{\sin h}{\sin r}\right). \quad (10)$$

Case 3. When $L_{PB} < r \leq L_{PC}$, $B_r(P) \cap \Delta PBC$ includes a spherical triangle ΔPBD_2 and a sector centered at P with cut points on $\widehat{PD_2}$ and \widehat{PC} , as shown in Fig.4(c). With Equations (A.3) and (1), we have

$$S(r) = [(\alpha_P - \omega_r + \alpha_B + \beta_r - \pi) + \omega_r(1 - \cos r)]R^2, \quad (11)$$

where $\alpha_B = \angle PBC$. $\omega_r = \angle D_2PC$, depending on the distance r , can be calculated as

$$\omega_r = \cos^{-1}[(\overrightarrow{OC} \times \overrightarrow{OP})^0 \cdot (\overrightarrow{OD_2} \times \overrightarrow{OP})^0] = \angle MPC - \alpha_r. \quad (12)$$

Case 4. When $r > L_{PC}$, $B_r(P) \cap \Delta PBC$ is the spherical triangle ΔPBC as shown in Fig.4(d). Thus we have

$$S(r) = \Omega. \quad (13)$$

After simplifications, $S(r)$ can be represented as

$$S(r) = \begin{cases} 0, & r \leq 0 \\ \alpha_P g_r R^2, & 0 < r \leq h \\ (\alpha_1 g_r + \eta[(\alpha_r + \beta_r - \pi/2) + (\alpha_2 - \alpha_r)g_r])R^2, & h < r \leq L_{PB} \\ ((\alpha_P + \alpha_B + \beta_r - \pi) - \omega_r \cos r)R^2, & L_{PB} < r \leq L_{PC} \\ \Omega, & r > L_{PC} \end{cases} \quad (14)$$

where $g_r = 1 - \cos r$. Apparently $r \geq 0$ in reality; we include a case for $r \leq 0$ in the above formula so that the domain of the CDF of r_0 can be extended to \mathbb{R} . Again, the CDF of $L_0(\Delta PBC)$ is $F_{L_0}(r) = \frac{S(r)}{\Omega}$; hence its PDF is $f_{L_0}(r) := \frac{S'(r)}{\Omega}$

given in the following equation

$$f_{L_0}(r) = \begin{cases} 0, & r \leq 0 \text{ or } r > L_{PC} \\ \frac{1}{\Omega} \alpha_P \sin r R^2, & 0 < r \leq h \\ \frac{1}{\Omega} \{\alpha_1 \sin r + \eta[\alpha'_r \cos r + \beta'_r + (\alpha_2 - \alpha_r) \sin r]\} R^2, & h < r \leq L_{PB} \\ \frac{1}{\Omega} [\beta'_r - \omega'_r \cos r + \omega_r \sin r] R^2, & L_{PB} < r \leq L_{PC} \end{cases} \quad (15)$$

Here α'_r , β'_r , and ω'_{r_0} are the derivatives of α_{r_0} , β_{r_0} , and ω_{r_0} w.r.t. r_0 , respectively. When $h \leq r \leq L_{PC}$,

$$\alpha'_r = \frac{\partial \alpha'_r}{\partial r} = \frac{\tan h}{\sin r \cos r \sqrt{\tan^2 r - \tan^2 h}}, \quad (16)$$

$$\beta'_r = \frac{\partial \beta'_r}{\partial r} = -\frac{\sin h \cos r}{\sin r \sqrt{\sin^2 r - \sin^2 h}}, \quad (17)$$

$$\omega'_r = -\alpha'_r. \quad (18)$$

3.2. Extension to Convex Spherical Polygons

In real world applications, researchers may be interested in the distribution of arc distance between a pre-specified internal point P to a point Q that is uniformly distributed in a spherical polygon Γ . If Γ is convex, it can be decomposed into a combination of spherical triangles pivoting at P as shown in Fig. 5, so we can extend the results we obtained in the previous section to this case.

To avoid confusion, we use L_1 instead of L_0 to represent the random arc distance L_{PQ} . The CDF of L_1 can be calculated based on the formulas in subsection 3.1.

A convex spherical polygon Γ with n edges can be segmented as n spherical triangles pivoting at an internal P . An illustration is given in Fig. 5, where Γ is a spherical heptagon with vertices B_1, B_2, \dots, B_7 that is decomposed into seven spherical triangles: $\Delta PB_1 B_2, \dots, \Delta PB_7 B_1$.

Based on construction, for $L_1(\Gamma, P)$ defined for a spherical polygon Γ with n vertices B_1, B_2, \dots, B_n and an internal point P , its CDF and PDF are

$$F_{L_1}(r) = P(L_{PQ} \leq r) = \frac{1}{|\Gamma|} \sum_{i=1}^n S_i(r), \quad f_{L_1}(r) = \frac{1}{|\Gamma|} \sum_{i=1}^n S'_i(r). \quad (19)$$

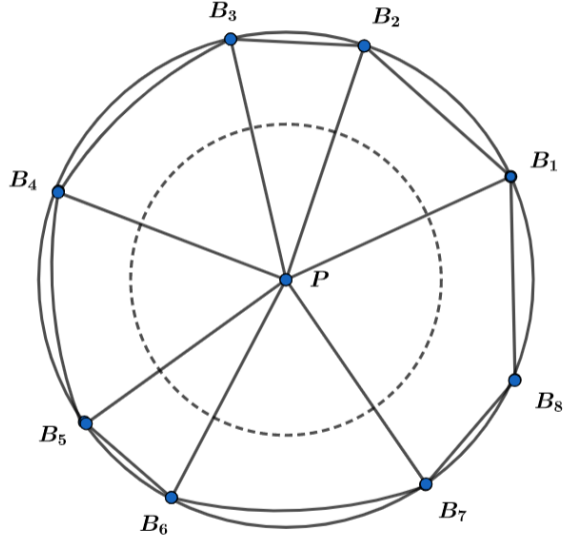


Figure 5: A convex spherical polygon Γ can be decomposed into a set of adjacent spherical triangles pivoting at a pre-specified internal point P . In Fig.5, the spherical cap centered at P represents a subset of Γ in which every point Q satisfies $L_{PQ} \leq r$, where r is the arc radius of this spherical cap. Apparently, this spherical cap is the disjoint union of spherical fans pertain to the member triangles. Consequently, the statistical properties of $L_1 = L_{PQ}$, the arc distance between P and a random point Q in Γ , can be derived from the properties of r_0 , which is the random arc distance between Q to a pre-selected vertex P of a spherical triangle.

where $S_i(r) = |B_r(P) \cap \Delta PB_i B_{i+1}|$, for $i = 1, 2, \dots, n - 1$, and $S_n(r) = |B_r(P) \cap \Delta PB_n B_1|$. These values, as well as their derivatives, can be computed by Equations (14) and (15). Of note, $S_i(r) = |\Delta PB_n B_1| \cdot P(L_{PQ} \leq r | Q \in \Delta PB_n B_1)$, therefore $F_{L_1}(r) = \sum_{i=1}^n \frac{|\Delta PB_n B_1|}{|\Gamma|} \cdot P(L_{PQ} \leq r | Q \in \Delta PB_n B_1)$, which is a weighted summation of conditional probabilities.

3.3. Distribution of the Minimal Arc Distance $L_2(P_1, \dots, P_m)$

Let $\{P_1, P_2, \dots, P_m\}$ be a pre-specified set of points on a sphere and Q be a random point that is uniformly distributed on this sphere. Let $L_2 :=$

$\min_{j=1}^m L_{P_j Q}$ be the minimal arc length between Q and $\{P_1, P_2, \dots, P_m\}$. To derive the distribution of L_2 , we first partition the sphere into $\{\Gamma_j\}_{j=1}^m$, the spherical Voronoi diagram with seeds $\{P_1, P_2, \dots, P_m\}$. By construction, each cell Γ_j in this diagram is a spherical polygon such that every point in Γ_j is closer to P_j (the seed of Γ_j) than any other seed in terms of arc distance. Consequently, if $Q \in \Gamma_j$, $L_2 = L_{P_j Q}$. This property is illustrated in Fig.6.

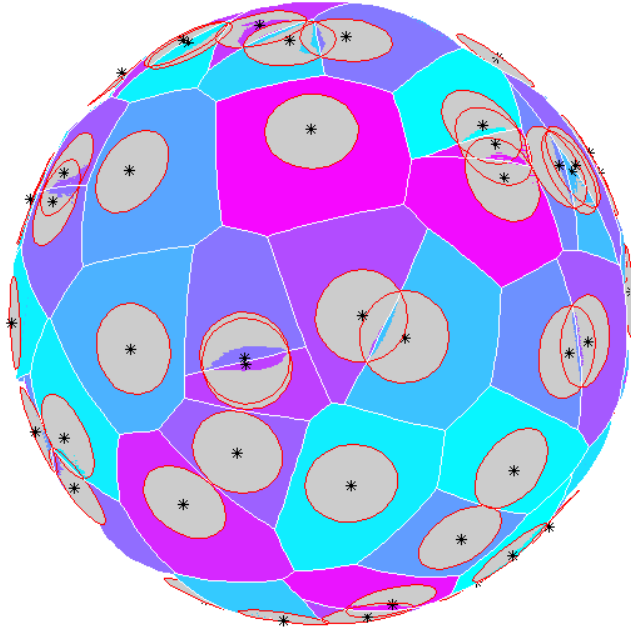


Figure 6: A spherical Voronoi diagram is a partition of sphere that consists of adjacent and disjoint spherical polygons ($\{\Gamma_1, \dots, \Gamma_m\}$) based on pre-specified seeds $\{P_1, \dots, P_m\}$. For each point $Q \in \Gamma_j$, its arc distance to P_j (the seed of Γ_j) is the shortest among all seeds. Circles in the figure represent points that have the same arc distance to a given seed. The intersections of these circles can be used to determine the boundaries between adjacent cells.

Once the Voronoi diagram is constructed, the distribution of L_2 can be derived in this way. First, we use Equation (19) to obtain the distribution of L_2 conditional on $Q \in \Gamma_j$. As a reminder, it depends on partition Γ_j into disjoint spherical triangles $\Delta P_j B_{i,j} B_{i+1,j}$, for $i = 1, 2, \dots, n_j$. The unconditional distribution of L_2 can then be obtained by taking the weighted summation of

these conditional distributions over all spherical triangles. The final result is presented as follows.

$$\begin{aligned}
F_{L_2}(r) &= \sum_{j=1}^m \frac{|\Gamma_j|}{4\pi R^2} \cdot F_{L_1}(r|Q \in \Gamma_j) = \frac{1}{4\pi R^2} \sum_{j=1}^m \sum_{i=1}^{n_j} S_{i,j}(r). \\
f_{L_2}(r) &= F'_{L_2}(r) = \frac{1}{4\pi R^2} \sum_{j=1}^m \sum_{i=1}^{n_j} S'_{i,j}(r).
\end{aligned} \tag{20}$$

Here $S_{i,j}(r) = |B_r(P) \cap \Delta P_j B_{i,j} B_{i+1,j}|$ is the intersection of a spherical ball and the spherical triangle $\Delta P_j B_{i,j} B_{i+1,j} \subset \Gamma_j$. It is easy to see that

$$\begin{aligned}
S_{i,j}(r) &= |\Delta P_j B_{i,j} B_{i+1,j}| \cdot P(L_{P_j Q} \leq r | Q \in \Delta P_j B_{i,j} B_{i+1,j}), \\
\sum_{i=1}^{n_j} S_{i,j}(r) &= |\Gamma_j| \cdot F_{L_1}(r|Q \in \Gamma_j).
\end{aligned}$$

4. Moments

With the density functions derived in the previous section (Equations (15), (19), and (20)), we are now ready to compute the k th moments of L_0 , L_1 , and L_3 .

For a given spherical triangle ΔPBC , we have

$$\begin{aligned}
E(L_0^k(\Delta PBC)) &= \int_{-\infty}^{\infty} r_0^k f_{L_0}(r_0) dr_0 := \frac{R^2}{\Omega} (\text{Term}_1 + \text{Term}_2 + \text{Term}_3). \\
\text{Term}_1 &= \int_0^h r_0^k \cdot \alpha_P \sin r_0 dr_0. \\
\text{Term}_2 &= \int_h^{L_{PB}} r_0^k (\alpha_1 \sin r_0 + \eta(\alpha'_{r_0} \cos r_0 + \beta'_{r_0} + (\alpha_2 - \alpha_{r_0}) \sin r_0)) dr_0. \\
\text{Term}_3 &= \int_{h_{PB}}^{L_{PC}} r_0^k \cdot (\beta'_{r_0} + \omega'_{r_0} \cos r_0 - \omega_{r_0} \sin r_0) dr_0.
\end{aligned} \tag{21}$$

Here α'_{r_0} and β'_{r_0} are sophisticated functions of r_0 defined by Equations (16) and (17). To the best of our knowledge, Equation (21) does not permit an analytic solution. In practice, it can be calculated with a suitable numerical integration method. In our implementation, this integral is computed by Gaussian quadrature [33].

As we mentioned in Section 3.2, moments of L_1 for a given convex spherical polygon Γ can be computed by first divide Γ into disjoint spherical triangles $\Delta P B_i B_{i+1}$ (see Figure 5), evaluate the moments of the corresponding L_0 in

each triangle (by Equation (21)), and then take the weighted summation of these conditional moments. In summary, we have

$$E(L_1^k(\Gamma)) = \frac{1}{|\Gamma|} \sum_{i=1}^n |\Delta P B_i B_{i+1}| \cdot E(L_0^k(\Delta P B_i B_{i+1})). \quad (22)$$

Likewise, the moments of L_2 for a given set of seeds $\{P_1, \dots, P_m\}$ can be obtained by first partition the sphere into m Voronoi cells Γ_j , and then take the weighted summation of the conditional moments of the corresponding L_1 within each Γ_j .

$$\begin{aligned} E(L_2^k(\{P_1, \dots, P_m\})) &= \frac{1}{4\pi R^2} \sum_{j=1}^m |\Gamma_j| \cdot E(L_1^k(\Gamma_j)) \\ &= \frac{1}{4\pi R^2} \sum_{j=1}^m \sum_{i=1}^n |\Delta P B_{i,j} B_{i+1,j}| \cdot E(L_0^k(\Delta P B_{i,j} B_{i+1,j})). \end{aligned} \quad (23)$$

Using similar techniques, we are able to derive several moments of cosine similarities $\cos(L_a^k)$, for $a = 0, 1, 2$ and $k = 1, 2, 4, 6$. These results are provided in Appendix B.

5. Numerical experiment

We conduct three sets of Monte Carlo experiments to verify the theoretical results derived in Section 4.

In each simulation, we first generate $m = 100$ random seeds $\{P_1, \dots, P_m\}$ on a unit sphere based on the algorithm defined in [34] which is numerically stable and more accurate than many popular spherical sampling method at generating points near the north and south poles. Technical details about these three simulations are provided as follows.

- Sim1: All $m = 100$ seeds are generated based on the uniform distribution on the unit sphere. This is one of the most commonly used model in applications such as wireless communications.
- Sim2: First, we sample 100 seeds on the sphere uniformly. For the first 75 of them, we reflect those in the lower hemisphere through the xy -plane to ensure that all of them are in the upper hemisphere. It can be shown

easily that these processed seeds are uniformly distributed on the upper hemisphere. Similarly, we use reflection to ensure the rest 25 are uniformly distributed on the lower hemisphere. We created this scenarios to mimic an unbalanced case in which the sites are denser in a subset of the sphere.

- Sim3: Using the acceptance-rejection method, we generate 50 seeds that are uniformly distributed on the North end region, and another 50 seeds uniformly distributed on the South end region. Here the North end region is defined as $\{(x, y, z) \in S^1 | z \geq 0.9\}$, which is the spherical cap near the north pole with height $h = 0.9$. The South end region is defined in a similar way: $\{(x, y, z) \in S^1 | z \leq -0.9\}$. We use this scenario to illustrate an extremely unbalanced case in which all seeds are concentrated on two relatively small and disjoint regions of the sphere.

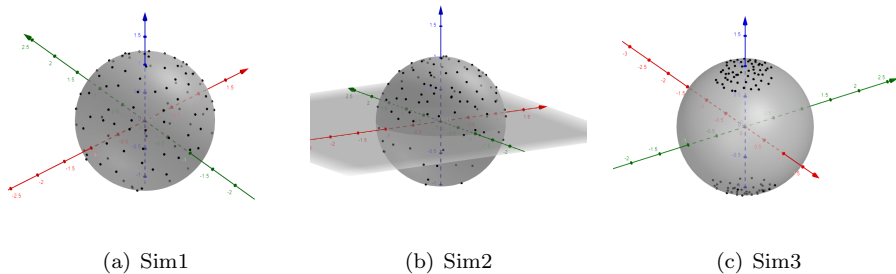


Figure 7: Three distributions of seeds used in simulations. (a) In Sim1, all $m = 100$ seeds are uniformly generated on the surface of the sphere. (b) In Sim2, the majority of the seeds (75 of them) are uniformly distributed on the upper hemisphere of the sphere, while the rest (25 of them) are uniformly distributed on the lower hemisphere. (c) In Sim3, half of the sites are uniformly generated on the North end region, while others are uniformly generated on the South end region.

In each case, once the seeds are generated, we uniformly sample 10, 000 points (Q s) on the sphere and compute $L_2 := \min_{j=1}^m L_{P_j Q}$, the shortest arc distance between Q and the nearest seed. We then compute the empirical moments of L_2 and $\cos L_2$ and compare them with their theoretical counterparts derived in Section 4.

To evaluate the discrepancy between the theoretical and empirical results, we use the Absolute Relative Error (ARE) define as follows

$$\text{ARE}(m) = \left| \frac{\hat{m} - m}{m} \right|. \quad (24)$$

Here \hat{m} is one of the sample moments reported in Table 1, and m is its corresponding oracle moment computed by our theoretical derivations. To further minimize the impact of random variations in those Monte Carlo experiments, all experiments are repeated for 100 times, and the mean, maximum, and standard deviation of the ARE reported in Table 1 are computed from these 100 repetitions, each consists of 10,000 randomly sampled Q on the unit sphere.

From Table 1, we find that the theoretical and empirical moments of L_2 and $\cos(L_2)$ match well in most of the cases. Specifically, the mean AREs for lower order moments of L_2 across different scenarios stay lower than 0.01; for higher order moments the mean AREs are all lower than 0.02. The max AREs for moments of L_2 are a little higher, but most of them are still lower than 0.05, except the 4th order moments of L_2 in Sim2 (0.064).

Estimated moments of cosine similarity have somewhat lower but acceptable accuracy. With a few exceptions, most of $E \cos^k L_2$ have mean and max ARE lower than 0.05. We believe the inflated ARE of these moments is largely due to the fact that the theoretical formulae of $E \cos^k L_2$ involves dozens of terms (e.g., Equation (B.16)), so the total numerical error, which is the sum of errors in all terms, becomes larger than that of $E(L_2^k)$.

Of note, the standard deviations of AREs are relatively low across all scenarios and moments: for most of the cases, $\text{STD}(\text{ARE}) \leq 0.01$. It implies that the reported accuracy is stable across 100 repetitions.

6. Conclusion & Discussion

In this paper, we first derive the CDF and PDF of $L_0(\Delta PBC)$, the arc distance between P , a vertex of the spherical triangle ΔPBC , to a uniformly distributed random interior point Q . Using a technique based on polygon decomposition, we are able to extend these results to cases in which the spherical

	Measurement	$E(L_2)$	$E(L_2^2)$	$E(L_2^3)$	$E(L_2^4)$	$E(\cos^2 L_2)$	$E(\cos^4 L_2)$	$E(\cos^6 L_2)$
Sim1	Proposed Method	0.176	0.039	0.010	0.003	0.962	0.926	0.893
	Mean MC	0.175	0.039	0.010	0.003	0.944	0.960	0.845
	Mean ARE	0.005	0.009	0.013	0.017	0.019	0.037	0.054
	Max ARE	0.014	0.026	0.038	0.050	0.027	0.050	0.071
	STD ARE	0.003	0.006	0.009	0.012	0.002	0.004	0.006
Sim2	Proposed Method	0.194	0.050	0.016	0.006	0.952	0.908	0.870
	Mean MC	0.195	0.050	0.016	0.006	0.980	0.958	0.938
	Mean ARE	0.005	0.009	0.014	0.020	0.029	0.055	0.078
	Max ARE	0.020	0.035	0.045	0.064	0.043	0.077	0.106
	STD ARE	0.004	0.007	0.010	0.015	0.004	0.007	0.010
Sim3	Proposed Method	0.380	0.208	0.133	0.091	0.820	0.704	0.625
	Mean MC	0.378	0.206	0.132	0.090	0.807	0.684	0.601
	Mean ARE	0.006	0.008	0.009	0.011	0.016	0.028	0.038
	Max ARE	0.013	0.017	0.018	0.019	0.024	0.041	0.055
	STD ARE	0.005	0.007	0.007	0.008	0.005	0.008	0.009

Table 1: Simulation results show that our proposed theoretical results matches well with the empirical estimation for moments of L_2 and $\cos L_2$ in all three scenarios. The mean AREs for lower order moments of L_2 across different scenarios stay lower than 0.01; for higher order moments the mean AREs are all lower than 0.02. The max AREs for moments of L_2 are a little higher, but most of them are still lower than 0.05, except the 4th order moments of L_2 in Sim2 (0.064). The estimation for $\cos L_2$ is less accurate, but still have low mean and max ARE for lower order moments. Most of the estimation for $\cos L_2$ have mean and max ARE lower than 0.05. In addition, the accuracy of the estimations is stable across different scenarios, with standard deviation of ARE ≤ 0.01 in most cases.

triangle is replaced by a convex spherical polygon ($L_1(\Gamma)$). Using methods developed for spherical Voronoi diagrams and integration techniques, we are able to compute arbitrary moments of $L_2(\{P_1, \dots, P_m\})$, the shortest arc distance from a uniformly distributed random point Q to a set of pre-defined seeds $\{P_1, \dots, P_m\}$ on a sphere. Finally, we compute moments for L_2 and $\cos L_2$, which are both widely used in various applications.

We conduct Monte Carlo simulations to validate our theoretical results. By and large, the theoretical and the empirical results are consistent. However, higher order moments for both L_2 and $\cos L_2$ have larger AREs than the lower moments. This is not beyond our expectation, since larger samples are required in order to obtain estimates of similar quality for higher order moments [35].

Note that the assumption of convexity of spherical polygon in deriving the CDF and PDF of L_1 is made out of convenience, not necessity. We believe the CDF/PDF of L_{PQ} , for Q uniformly distributed in an arbitrary spherical triangle Δ of which $P \notin \Delta$, can be derived based on techniques we deployed in this study. Since it is always possible to divide a non-convex spherical polygon into disjoint spherical triangles (not necessarily pivoting at a pre-specified interior point P if it is not convex), we can aggregate the CDF/PDF with exterior point P to obtain the desired formula for a non-convex polygon. Furthermore, every smooth geometric object O on S^2 can be approximated by spherical polygons therefore a disjoint union of spherical triangles Δ_j . Therefore, the distribution of the arc distance between an arbitrary pre-specified point $P \in S^2$ and Q uniformly distributed on O can be approximated by our method. How to achieve the best accuracy of the said approximation with a fixed number of spherical triangles/polygons, therefore attain the best trade-off between computational cost and accuracy, is an interesting research topic that warrants a future study.

We think our work has tangible practical impact in many applications. The statistical distribution of the minimal distance between random points and a pre-specified seeds (sites) is used in wireless communications, forest ecology, etc. Most existing studies in this field are based on the Voronoi diagram in \mathbb{R}^2 . For large-scale studies, it may be necessary to model the domain as a

sphere because the curvature of earth may become non-negligible. Our results has potential to significantly improve the accuracy of the results under these scenarios.

Last but not least, many intermediate results (e.g., the distribution of L_0 and L_1) and mathematical techniques (e.g., the partition of the spherical triangles and their classifications) we developed in this study may help other researchers study similar problems in the future.

References

- [1] J. M. Augenbaum, C. S. Peskin, On the construction of the voronoi mesh on a sphere, *Journal of Computational Physics* 59 (2) (1985) 177–192 (1985).
- [2] H. Edelsbrunner, R. Seidel, Voronoi diagrams and arrangements, *Discrete & Computational Geometry* 1 (1) (1986) 25–44 (1986).
- [3] F. Aurenhammer, Voronoi diagrams—a survey of a fundamental geometric data structure, *ACM Computing Surveys (CSUR)* 23 (3) (1991) 345–405 (1991).
- [4] M. de Berg, M. Van Kreveld, O. Schwarzkopf, M. Overmars, *Computational geometry algorithms and applications*, 2nd Edition, Springer, Germany, 2000 (2000).
- [5] O. Persson, Distance methods: the use of distance measurements in the estimation of seedling density and open space frequency, *Studia forestalia suecica* (15) (1964) 1–68 (1964).
- [6] N. Christofides, S. Eilon, Expected distances in distribution problems, *Journal of the Operational Research Society* 20 (4) (1969) 437–443 (1969).
- [7] I. I. Vaisman, Statistical and computational geometry of biomolecular structure, in: *Handbook of Computational Statistics*, Springer, 2012, pp. 1095–1112 (2012).

- [8] G. Zhao, K. Xuan, W. Rahayu, D. Taniar, M. Safar, M. Gavrilova, B. Srinivasan, Voronoi-based continuous nearest neighbor search in mobile navigation, *Industrial Electronics, IEEE Transactions on* 58 (6) (2011) 2247–2257 (2011).
- [9] J. Köll, S. Hallström, Generation of periodic stochastic foam models for numerical analysis, *Journal of cellular plastics* 50 (1) (2014) 37–54 (2014).
- [10] J. Lin, Divergence measures based on the shannon entropy, *IEEE Transactions on Information theory* 37 (1) (1991) 145–151 (1991).
- [11] A. Villagran, G. Huerta, M. Vannucci, C. S. Jackson, A. Nosedal, Non-parametric sampling approximation via voronoi tessellations, *Communications in Statistics - Simulation and Computation* 45 (2) (2016) 717–736 (2016).
- [12] A. Okabe, B. Boots, K. Sugihara, S. N. Chiu, *Spatial tessellations: concepts and applications of Voronoi diagrams*, Vol. 501, John Wiley & Sons, 2009 (2009).
- [13] H. Li, X. Qiu, Moments of distance from a vertex to a uniformly distributed random point within arbitrary triangles, *Mathematical Problems in Engineering* 2016 (2016).
- [14] F. Aurenhammer, H. Edelsbrunner, An optimal algorithm for constructing the weighted voronoi diagram in the plane, *Pattern Recognition* 17 (2) (1984) 251–257 (1984).
- [15] R. Pure, S. Durrani, Computing exact closed-form distance distributions in arbitrarily shaped polygons with arbitrary reference point, *The Mathematica Journal* (2015).
URL dx.doi.org/doi:10.3888/tmj.17-6
- [16] M. Ahmadi, J. Pan, Random distances associated with arbitrary triangles: A recursive approach with an arbitrary reference point, *UVicSpace* (2014).
URL <http://hdl.handle.net/1828/5134>

- [17] A. Okabe, A. Suzuki, Locational optimization problems solved through voronoi diagrams, *European Journal of Operational Research* 98 (3) (1997) 445–456 (1997).
- [18] Q. Du, M. D. Gunzburger, L. Ju, Voronoi-based finite volume methods, optimal voronoi meshes, and pdes on the sphere, *Computer methods in applied mechanics and engineering* 192 (35-36) (2003) 3933–3957 (2003).
- [19] L. Hashemi Beni, M. A. Mostafavi, J. Pouliot, M. Gavrilova, Toward 3d spatial dynamic field simulation within gis using kinetic voronoi diagram and delaunay tetrahedralization, *International Journal of Geographical Information Science* 25 (1) (2011) 25–50 (2011).
- [20] H. Hu, X. Liu, P. Hu, Voronoi diagram generation on the ellipsoidal earth, *Computers & geosciences* 73 (2014) 81–87 (2014).
- [21] H.-S. Na, C.-N. Lee, O. Cheong, Voronoi diagrams on the sphere, *Computational Geometry* 23 (2) (2002) 183–194 (2002).
- [22] S. Chaidee, K. Sugihara, Approximation of fruit skin patterns using spherical voronoi diagrams, *Pattern Analysis and Applications* 20 (3) (2017) 783–795 (2017).
- [23] S. Chaidee, K. Sugihara, Spherical laguerre voronoi diagram approximation to tessellations without generators, *Graphical Models* 95 (2018) 1–13 (2018).
- [24] R. Bauer, Distribution of points on a sphere with application to star catalogs, *Journal of Guidance, Control, and Dynamics* 23 (1) (2000) 130–137 (2000).
- [25] J. Beck, Sums of distances between points on a sphere—an application of the theory of irregularities of distribution to discrete geometry, *Mathematika* 31 (1) (1984) 33–41 (1984).

- [26] K. Lochmann, L. Oger, D. Stoyan, Statistical analysis of random sphere packings with variable radius distribution, *Solid State Sciences* 8 (12) (2006) 1397–1413 (2006).
- [27] T. Cai, J. Fan, T. Jiang, Distributions of angles in random packing on spheres, *The Journal of Machine Learning Research* 14 (1) (2013) 1837–1864 (2013).
- [28] I. S. Dhillon, D. S. Modha, Concept decompositions for large sparse text data using clustering, *Machine learning* 42 (1-2) (2001) 143–175 (2001).
- [29] X. Qiu, S. Wu, H. Wu, A new information criterion based on langevin mixture distribution for clustering circular data with application to time course genomic data, *Statistica Sinica* (2015) 1459–1476 (2015).
- [30] H. V. Nguyen, L. Bai, Cosine similarity metric learning for face verification, in: *Asian conference on computer vision*, Springer, 2010, pp. 709–720 (2010).
- [31] J. Ye, Cosine similarity measures for intuitionistic fuzzy sets and their applications, *Mathematical and computer modelling* 53 (1-2) (2011) 91–97 (2011).
- [32] G. Van Brummelen, *Heavenly mathematics: The forgotten art of spherical trigonometry*, Princeton University Press, 2012 (2012).
- [33] G. H. Golub, J. H. Welsch, Calculation of gauss quadrature rules, *Mathematics of computation* 23 (106) (1969) 221–230 (1969).
- [34] G. Marsaglia, et al., Choosing a point from the surface of a sphere, *The Annals of Mathematical Statistics* 43 (2) (1972) 645–646 (1972).
- [35] G. Casella, R. L. Berger, *Statistical inference*, Vol. 2, Duxbury Pacific Grove, CA, 2002 (2002).

Appendix A. Definitions of useful geometric concepts of spherical triangles

$$L_{AB} = R\varphi_{AB} \quad (\text{A.1})$$

The area of the spherical cap, as shown in Fig. 2(a), is

$$A_{cap} = 2\pi R^2(1 - \cos \theta) \quad (\text{A.2})$$

The area of the spherical sector, as shown in Fig. 2(b), is

$$A_{fan} = \alpha R^2(1 - \cos \theta) \quad (\text{A.3})$$

Appendix B. Moments of Cosine Similarity

With the PDF of L_2 provided in Equation (15), we can calculate the mathematical expectation of $\cos^2 L_2$ as follows.

$$\begin{aligned} E(\cos^2(r)) &= \int_{-\infty}^{\infty} \cos^2(r) f(r) dr \\ &= \frac{1}{\Omega} \left(\int_0^h \cos^2(r) \cdot \alpha_P \sin r dr \right. \\ &\quad + \int_h^{L_{PB}} \cos^2(r) \cdot \{ \alpha_1 \sin r + \eta [\alpha'_r \cos r + \beta'_r + (\alpha_2 - \alpha_r) \sin r] \} dr \\ &\quad + \left. \int_{h_{PB}}^{L_{PC}} \cos^2(r) \cdot [\beta'_r + \omega'_r \cos r - \omega_r \sin r] dr \right) \\ &= \frac{1}{\Omega} (\text{Term}_1 + \text{Term}_2 + \text{Term}_3). \end{aligned} \quad (\text{B.1})$$

The first two terms in the above equation are derived as follows.

$$\begin{aligned} \text{Term}_1 &= \int_0^h \cos^2(r) \cdot \alpha_P \sin r dr = \frac{-1}{3} \alpha_P \cdot \cos^3(r) \Big|_0^h \\ &= \frac{-1}{3} \alpha_P \cdot (\cos^3(h) - 1) = \frac{1}{3} \alpha_P (1 - \cos^3(h)). \end{aligned} \quad (\text{B.2})$$

$$\begin{aligned}
\text{Term}_2 &= \int_h^{L_{PB}} \cos^2(r) \cdot \{\alpha_1 \sin r + \eta[\alpha'_r \cos r + \beta'_r + (\alpha_2 - \alpha_r) \sin r]\} dr \\
&= \int_h^{L_{PB}} \cos^2(r) \cdot \alpha_1 \sin r dr + \eta I_\eta \\
&= \frac{1}{3} \alpha_1 [\cos^3(h) - \cos^3(h_{PB})] + \eta I_\eta.
\end{aligned} \tag{B.3}$$

Here

$$\begin{aligned}
I_\eta &= \int_h^{L_{PB}} \cos^2(r) [\alpha'_r \cos r + \beta'_r + (\alpha_2 - \alpha_r) \sin r] dr \\
&= \int_h^{L_{PB}} (\cos^3 r \alpha'_r - \cos^2 r \sin r \alpha_r) dr + \int_h^{L_{PB}} \cos^2 r \beta'_r dr \\
&\quad + \int_h^{L_{PB}} \alpha_2 \cos^2 r \sin r dr = I_{\eta,1} + I_{\eta,2} + I_{\eta,3},
\end{aligned} \tag{B.4}$$

where

$$\begin{aligned}
I_{\eta,1} &= \int_h^{L_{PB}} (\cos^3 r \alpha'_r - \cos^2 r \sin r \alpha_r) dr \\
&= \frac{1}{3} \alpha_r \cos^3 r \Big|_h^{L_{PB}} + \frac{2}{3} \int_h^{L_{PB}} \cos^3 r \alpha'_r dr \\
&= \frac{1}{3} \left[\arccos \frac{\tan h}{\tan L_{PB}} \cos^3 L_{PB} - 0 \right] + \frac{2}{3} \int_h^{L_{PB}} \frac{\tan h \cos^2 r}{\sin r \sqrt{\tan^2 r - \tan^2 h}} dr \\
&= \frac{1}{3} \arccos \frac{\tan h}{\tan L_{PB}} \cos^3 L_{PB} + \frac{2}{3} \cdot I_{\eta,1p}.
\end{aligned} \tag{B.5}$$

$$\begin{aligned}
I_{\eta,1p} &= \int_h^{L_{PB}} \frac{\tan h \cos^2 r}{\sin r \sqrt{\tan^2 r - \tan^2 h}} dr \\
&= \tan h \left(\int_h^{L_{PB}} \frac{1}{\sin r \sqrt{\tan^2 r - \tan^2 h}} dr - \int_h^{L_{PB}} \frac{\sin r}{\sqrt{\tan^2 r - \tan^2 h}} dr \right) \\
&= -\frac{1}{2} \arctan \frac{2 \tan h \sqrt{\tan^2 r - \tan^2 h} \sqrt{\tan^2 r + 1}}{\tan^2 r - \tan^2 r \tan^2 h - 2 \tan^2 h} \Big|_h^{L_{PB}} \\
&\quad - \frac{\sqrt{\tan^2 r - \tan^2 h}}{\tan h (1 + \tan^2 h) \sqrt{1 + \tan^2 r}} \Big|_h^{L_{PB}} \\
&= -\frac{1}{2} \arctan \frac{2 \tan h \sqrt{\tan^2 L_{PB} - \tan^2 h} \sqrt{\tan^2 L_{PB} + 1}}{\tan^2 L_{PB} - \tan^2 L_{PB} \tan^2 h - 2 \tan^2 h} \\
&\quad - \frac{\tan h \sqrt{\tan^2 L_{PB} - \tan^2 h}}{(1 + \tan^2 h) \sqrt{1 + \tan^2 L_{PB}}}.
\end{aligned} \tag{B.6}$$

Note that the following two technical results are needed in deriving the above

integral. Let $u = \tan r$, $a = \tan h$, we have

$$\begin{aligned}
& \int \frac{1}{\sin r \sqrt{\tan^2 r - \tan^2 h}} dr = \int \frac{1}{u \sqrt{u^2 - a^2} \sqrt{1 + u^2}} du \\
& = \frac{\sqrt{-a^2}}{2a^2} \left[\ln \frac{\sqrt{u^2 + 1} - 1}{\sqrt{-a^2} - \sqrt{u^2 - a^2}} - \ln(\sqrt{-a^2}) \right. \\
& \quad \left. + \frac{\sqrt{u^2 + 1} - 1}{\sqrt{-a^2} - \sqrt{u^2 - a^2}} - \frac{a^2(\sqrt{u^2 + 1} - 1)}{\sqrt{-a^2} - \sqrt{u^2 - a^2}} + \frac{\sqrt{-a^2}(\sqrt{u^2 + 1} - 1)^2}{(\sqrt{-a^2} - \sqrt{u^2 - a^2})^2} \right] \\
& = \frac{i}{2a} \ln \frac{u^2 - u^2 a^2 - 2a^2 + i \cdot 2a \sqrt{u^2 - a^2} \sqrt{u^2 + 1}}{u^2 (a^2 + 1)^2} \\
& = -\frac{1}{2a} \arctan \frac{2a \sqrt{u^2 - a^2} \sqrt{u^2 + 1}}{u^2 - u^2 a^2 - 2a^2} + \text{Const}, \\
\text{Const} & := \begin{cases} -\frac{i}{2a} \ln(a^2 + 1), & u^2 - u^2 a^2 - 2a^2 > 0, \\ -\frac{i}{2a} \ln(a^2 + 1) - \frac{\pi}{2a}, & u^2 - u^2 a^2 - 2a^2 < 0. \end{cases}
\end{aligned} \tag{B.7}$$

Note that only the first term of the results in Equation (B.7) depends on variable $u := \tan r$, so the choice of Const is irrelevant in computing the corresponding definite integral used in Equation (B.6).

Again let $u = \tan^2 r$, $b = \tan^2 h$, we have

$$\begin{aligned}
& \int \frac{\sin r}{\sqrt{\tan^2 r - \tan^2 h}} dr = \int \frac{1}{2\sqrt{u-b}(1+u)^{3/2}} du \\
& = \frac{\sqrt{u-b}}{(b+1)\sqrt{u+1}} = \frac{\sqrt{\tan^2 r - \tan^2 h}}{(1 + \tan^2 h)\sqrt{1 + \tan^2 r}}.
\end{aligned} \tag{B.8}$$

The rest two terms, $I_{\eta,2}, I_{\eta,3}$ are provided as follows.

$$\begin{aligned}
I_{\eta,2} & = \int_h^{L_{PB}} \cos^2 r \beta'_r dr = - \int_h^{L_{PB}} \frac{\sin h \cos^3 r}{\sin r \sqrt{\sin^2 r - \sin^2 h}} dr \\
& = -(\arctan \frac{\sqrt{\sin^2 r - \sin^2 h}}{\sin h} - \sin h \sqrt{\sin^2 r - \sin^2 h}) \Big|_h^{L_{PB}} \\
& = \sin h \sqrt{\sin^2 L_{PB} - \sin^2 h} - \arctan \frac{\sqrt{\sin^2 L_{PB} - \sin^2 h}}{\sin h}.
\end{aligned} \tag{B.9}$$

$$\begin{aligned}
I_{\eta,3} & = \int_h^{L_{PB}} \alpha_2 \cos^2 r \sin r dr = -\frac{1}{3} \alpha_2 \cos^3 r \Big|_h^{L_{PB}} \\
& = \frac{1}{3} \alpha_2 (\cos^3 h - \cos^3 L_{PB}).
\end{aligned} \tag{B.10}$$

In summary, we have

$$\begin{aligned}
I_\eta &= I_{\eta,1} + I_{\eta,2} + I_{\eta,3} \\
&= \frac{1}{3} \arccos \frac{\tan h}{\tan L_{PB}} \cos^3 L_{PB} - \frac{1}{3} \arctan \frac{2 \tan h \sqrt{\tan^2 L_{PB} - \tan^2 h} \sqrt{\tan^2 L_{PB} + 1}}{\tan^2 L_{PB} - \tan^2 L_{PB} \tan^2 h - 2 \tan^2 h} \\
&\quad - \frac{2 \tan h \sqrt{\tan^2 L_{PB} - \tan^2 h}}{3(1 + \tan^2 h) \sqrt{1 + \tan^2 L_{PB}}} + \sin h \sqrt{\sin^2 L_{PB} - \sin^2 h} \\
&\quad - \arctan \frac{\sqrt{\sin^2 L_{PB} - \sin^2 h}}{\sin h} + \frac{1}{3} \alpha_2 (\cos^3 h - \cos^3 L_{PB}).
\end{aligned} \tag{B.11}$$

Term₃ is derived as follows.

$$\begin{aligned}
\text{Term}_3 &= \int_{L_{PB}}^{L_{PC}} \cos^2(r) \cdot [\beta'_r + \omega'_r \cos r - \omega_r \sin r] dr \\
&= - \int_{L_{PB}}^{L_{PC}} \frac{\sin h \cos^3 r}{\sin r \sqrt{\sin^2 r - \sin^2 h}} dr + \frac{1}{3} \omega_r \cos^3 r \Big|_{L_{PB}}^{L_{PC}} - \frac{2}{3} \int_{L_{PB}}^{L_{PC}} \omega'_r \cos^3 r dr \\
&= \sin h \sqrt{\sin^2 L_{PC} - \sin^2 h} - \arctan \frac{\sqrt{\sin^2 L_{PC} - \sin^2 h}}{\sin h} \\
&\quad - \sin h \sqrt{\sin^2 L_{PB} - \sin^2 h} + \arctan \frac{\sqrt{\sin^2 L_{PB} - \sin^2 h}}{\sin h} \\
&\quad + \frac{1}{3} \left[\cos^3 L_{PB} \arccos \frac{\tan h}{\tan L_{PB}} - \cos^3 L_{PC} \arccos \frac{\tan h}{\tan L_{PC}} \right] \\
&\quad + \frac{2}{3} \int_{L_{PB}}^{L_{PC}} \cos^3 r \alpha'_r dr \\
&= \sin h \sqrt{\sin^2 L_{PC} - \sin^2 h} - \arctan \frac{\sqrt{\sin^2 L_{PC} - \sin^2 h}}{\sin h} \\
&\quad - \sin h \sqrt{\sin^2 L_{PB} - \sin^2 h} + \arctan \frac{\sqrt{\sin^2 L_{PB} - \sin^2 h}}{\sin h} \\
&\quad + \frac{1}{3} \cos^3 L_{PB} \arccos \frac{\tan h}{\tan L_{PB}} - \frac{1}{3} \cos^3 L_{PC} \arccos \frac{\tan h}{\tan L_{PC}} + \frac{2}{3} \text{Term}_4.
\end{aligned} \tag{B.12}$$

Using Equation (B.6), we have

$$\begin{aligned}
\text{Term}_4 &= \int_{L_{PB}}^{L_{PC}} \cos^3 r \alpha'_r dr = \int_{L_{PB}}^{L_{PC}} \frac{\tan h \cos^2 r}{\sin r \sqrt{\tan^2 r - \tan^2 h}} dr \\
&= \frac{1}{2} \arctan \frac{2 \tan h \sqrt{\tan^2 L_{PB} - \tan^2 h} \sqrt{\tan^2 L_{PB} + 1}}{\tan^2 L_{PB} - \tan^2 L_{PB} \tan^2 h - 2 \tan^2 h} \\
&\quad - \frac{1}{2} \arctan \frac{2 \tan h \sqrt{\tan^2 L_{PC} - \tan^2 h} \sqrt{\tan^2 L_{PC} + 1}}{\tan^2 L_{PC} - \tan^2 L_{PC} \tan^2 h - 2 \tan^2 h} \\
&\quad - \frac{\tan h \sqrt{\tan^2 L_{PC} - \tan^2 h}}{(1 + \tan^2 h) \sqrt{1 + \tan^2 L_{PC}}} + \frac{\tan h \sqrt{\tan^2 L_{PB} - \tan^2 h}}{(1 + \tan^2 h) \sqrt{1 + \tan^2 L_{PB}}}.
\end{aligned} \tag{B.13}$$

In summary, we have

$$\begin{aligned}
E(\cos^2(r)) &= \frac{1}{\Omega} (\text{Term}_1 + \text{Term}_2 + \text{Term}_3) \\
&= \frac{1}{3} \alpha_P (1 - \cos^3(h)) + \frac{1}{3} \alpha_1 [\cos^3(h) - \cos^3(h_{PB})] + \eta I_\eta \\
&\quad + \sin h \sqrt{\sin^2 L_{PC} - \sin^2 h} - \arctan \frac{\sqrt{\sin^2 L_{PC} - \sin^2 h}}{\sin h} \\
&\quad - \sin h \sqrt{\sin^2 L_{PB} - \sin^2 h} + \arctan \frac{\sqrt{\sin^2 L_{PB} - \sin^2 h}}{\sin h} \\
&\quad + \frac{1}{3} \cos^3 L_{PB} \arccos \frac{\tan h}{\tan L_{PB}} - \frac{1}{3} \cos^3 L_{PC} \arccos \frac{\tan h}{\tan L_{PC}} + \frac{2}{3} \text{Term}_4 \\
&= \frac{1}{3} \alpha_P (1 - \cos^3(h)) + \frac{1}{3} \alpha_1 [\cos^3(h) - \cos^3(h_{PB})] \\
&\quad + \left(\frac{1}{3} \arccos \frac{\tan h}{\tan L_{PB}} \cos^3 L_{PB} \right. \\
&\quad - \frac{1}{3} \arctan \frac{2 \tan h \sqrt{\tan^2 L_{PB} - \tan^2 h} \sqrt{\tan^2 L_{PB} + 1}}{\tan^2 L_{PB} - \tan^2 L_{PB} \tan^2 h - 2 \tan^2 h} \\
&\quad - \frac{2 \tan h \sqrt{\tan^2 L_{PB} - \tan^2 h}}{3(1 + \tan^2 h) \sqrt{1 + \tan^2 L_{PB}}} + \sin h \sqrt{\sin^2 L_{PB} - \sin^2 h} \\
&\quad \left. - \arctan \frac{\sqrt{\sin^2 L_{PB} - \sin^2 h}}{\sin h} + \frac{1}{3} \alpha_2 (\cos^3 h - \cos^3 L_{PB}) \right) \\
&\quad + \sin h \sqrt{\sin^2 L_{PC} - \sin^2 h} - \arctan \frac{\sqrt{\sin^2 L_{PC} - \sin^2 h}}{\sin h} \\
&\quad - \sin h \sqrt{\sin^2 L_{PB} - \sin^2 h} + \arctan \frac{\sqrt{\sin^2 L_{PB} - \sin^2 h}}{\sin h} \\
&\quad + \frac{1}{3} \cos^3 L_{PB} \arccos \frac{\tan h}{\tan L_{PB}} - \frac{1}{3} \cos^3 L_{PC} \arccos \frac{\tan h}{\tan L_{PC}} \\
&\quad + \frac{1}{3} \arctan \frac{2 \tan h \sqrt{\tan^2 L_{PB} - \tan^2 h} \sqrt{\tan^2 L_{PB} + 1}}{\tan^2 L_{PB} - \tan^2 L_{PB} \tan^2 h - 2 \tan^2 h} \\
&\quad - \frac{1}{3} \arctan \frac{2 \tan h \sqrt{\tan^2 L_{PC} - \tan^2 h} \sqrt{\tan^2 L_{PC} + 1}}{\tan^2 L_{PC} - \tan^2 L_{PC} \tan^2 h - 2 \tan^2 h} \\
&\quad - \frac{2 \tan h \sqrt{\tan^2 L_{PC} - \tan^2 h}}{3(1 + \tan^2 h) \sqrt{1 + \tan^2 L_{PC}}} + \frac{2 \tan h \sqrt{\tan^2 L_{PB} - \tan^2 h}}{3(1 + \tan^2 h) \sqrt{1 + \tan^2 L_{PB}}}.
\end{aligned} \tag{B.14}$$

Similarly, we derive the expectation of $\cos^4 r$ and $\cos^6 r$ as follows.

$$\begin{aligned}
E(\cos^4 L_2) &= \int_{-\infty}^{+\infty} \cos^4 r \cdot f(r) dr \\
&= \frac{1}{\Omega} \left(\int_0^h \cos^4 r \cdot \alpha \alpha_p \sin r dr \right. \\
&\quad + \int_h^{L_{PB}} \cos^4 r \cdot \{ \alpha_1 \sin r + \eta [\alpha' \cos r + \beta' + (\alpha_2 - \alpha_r) \sin r] \} dr \\
&\quad \left. + \int_{L_{PB}}^{L_{PC}} \cos^4 r \cdot [\beta' + \omega' \cos r - \omega_r \sin r] dr \right) \\
&= \frac{1}{\Omega} \left(\frac{1}{5} \left(\angle MPC \cos^5(L_{PC}) - (\angle MPC + \alpha_2 \eta + \alpha_1) \cos^5(L_{PB}) + (\alpha_2 \eta - \alpha_p + \alpha_1) \cos^5 h + \alpha_p \right) \right. \\
&\quad + \frac{4\eta - 6}{5} \arctan \left(\frac{\sqrt{\cos^2 h - \cos^2(L_{PB})}}{\sin h} \right) + \frac{6}{5} \arctan \left(\frac{\sqrt{\cos^2 h - \cos^2(L_{PC})}}{\sin h} \right) \\
&\quad + \frac{4\eta - 6}{15} \sin h \left(\sin^2(L_{PB}) - 2 \cos^2 h - 4 \right) \sqrt{\cos^2 h - \cos^2(L_{PB})} \\
&\quad + \frac{2}{5} \sin h \left(\sin^2(L_{PC}) - 2 \cos^2 h - 4 \right) \sqrt{\cos^2 h - \cos^2(L_{PC})} \\
&\quad + (\eta - 1) \arcsin \left(\frac{\sin h}{|\sin(L_{PB})|} \right) + \arcsin \left(\frac{\sin h}{|\sin(L_{PC})|} \right) - \eta \arcsin \left(\frac{\sin h}{|\sin h|} \right) \\
&\quad - \frac{1}{5} \left(\cos^5(L_{PC}) \arccos \left(\frac{\tan h}{\tan(L_{PC})} \right) - (1 + \eta) \cos^5(L_{PB}) \arccos \left(\frac{\tan h}{\tan(L_{PB})} \right) \right) \\
&\quad - \frac{\eta - 1}{3} \sin h \sqrt{(\sin(L_{PB}) - \sin h)(\sin(L_{PB}) + \sin h)} (\sin^2(L_{PB}) + 2 \sin^2 h - 6) \\
&\quad \left. - \frac{1}{3} \sin h \sqrt{(\sin(L_{PC}) - \sin h)(\sin(L_{PC}) + \sin h)} (\sin^2(L_{PC}) + 2 \sin^2 h - 6) \right).
\end{aligned}$$

(B.15)

$$\begin{aligned}
E(\cos^6 r) &= \int_{-\infty}^{+\infty} \cos^6 r \cdot f(r) dr \\
&= \frac{1}{\Omega} \left(\int_0^h \cos^6 r \cdot \alpha_p \sin r dr \right. \\
&\quad + \int_h^{L_{PB}} \cos^6 r \cdot \{ \alpha_1 \sin r + \eta [\alpha' \cos r + \beta' + (\alpha_2 - \alpha_r) \sin r] \} dr \\
&\quad + \int_{L_{PB}}^{L_{PC}} \cos^6 r \cdot [\beta' + \omega' \cos r - \omega_r \sin r] dr \Big) \\
&= \frac{1}{\Omega} \left(\frac{1}{7} (\cos^7 h (\alpha_1 \eta - \alpha_p + \alpha_1) - \cos^7(L_{PB}) (\alpha_2 \eta - \angle MPC + \alpha_1) + \angle MPC \cos^7(L_{PC}) + \alpha_p) \right. \\
&\quad + \frac{6\eta - 8}{7} \arctan \left(\frac{\sqrt{\cos^2 h - \cos^2(L_{PB})}}{\sin h} \right) + \frac{8}{7} \arctan \left(\frac{\sqrt{\cos^2 h - \cos^2(L_{PC})}}{\sin h} \right) \\
&\quad - \frac{6\eta - 8}{105} \sin h \sqrt{\cos^2 h - \cos^2(L_{PB})} (\sin^2(L_{PB}) (\sin^2(L_{PB}) - 4 \cos^2 h - 11) + 8 \cos^4 h + 14 \cos^2 h + 23) \\
&\quad - \frac{8}{105} \sin h \sqrt{\cos^2 h - \cos^2(L_{PC})} (\sin^2(L_{PC}) (3 \sin^2(L_{PC}) - 4 \cos^2 h - 11) + 8 \cos^4 h + 14 \cos^2 h + 23) \\
&\quad + (\eta - 1) \arcsin \left(\frac{\sin h}{|\sin(L_{PB})|} \right) + \arcsin \left(\frac{\sin h}{|\sin(L_{PC})|} \right) - \eta \arcsin \left(\frac{\sin h}{|\sin h|} \right) \\
&\quad + \frac{1}{7} \left((1 + \eta) \cos^7(L_{PB}) \arccos \left(\frac{\tan h}{\tan(L_{PB})} \right) - \cos^7(L_{PC}) \arccos \left(\frac{\tan h}{\tan(L_{PC})} \right) \right) \\
&\quad + \frac{\eta - 1}{15} \sin h \sqrt{(\sin^2(L_{PB}) - \sin^2 h) (3 \sin^4(L_{PB}) + (4 \sin^2 h - 15) \sin^2(L_{PB}) + 8 \sin^4 h - 30 \sin^2 h + 45)} \\
&\quad + \frac{1}{15} \sin h \sqrt{(\sin^2(L_{PC}) - \sin^2 h) (3 \sin^4(L_{PC}) + (4 \sin^2 h - 15) \sin^2(L_{PC}) + 8 \sin^4 h - 30 \sin^2 h + 45)} \Big).
\end{aligned} \tag{B.16}$$